TU Delft

Delft University of Technology

A wavelet-based separation method for tonal and broadband components of low Reynolds-number propeller noise

Meloni, S.; de Paola, E.; Grande, E.; Ragni, D.; Stoica, L. G.; Di Marco, A.; Camussi, R.

DOI
10.1088/1361-6501/acb071

Publication date
2023

Document Version
Final published version

Published in
Measurement Science and Technology

Citation (APA)
Meloni, S., de Paola, E., Grande, E., Ragni, D., Stoica, L. G., Di Marco, A., & Camussi, R. (2023). A wavelet-based separation method for tonal and broadband components of low Reynolds-number propeller noise. *Measurement Science and Technology*, *34*(4), Article 044007. https://doi.org/10.1088/1361-6501/acb071

Important note
To cite this publication, please use the final published version (if applicable).
Please check the document version above.

Copyright
Other than for strictly personal use, it is not permitted to download, forward or distribute the text or part of it, without the consent of the author(s) and/or copyright holder(s), unless the work is under an open content license such as Creative Commons.

Takedown policy
Please contact us and provide details if you believe this document breaches copyrights.
We will remove access to the work immediately and investigate your claim.

This work is downloaded from Delft University of Technology.
For technical reasons the number of authors shown on this cover page is limited to a maximum of 10.

PAPER

A wavelet-based separation method for tonal and broadband components of low Reynolds-number propeller noise

To cite this article: S Meloni *et al* 2023 *Meas. Sci. Technol.* **34** 044007

View the article online for updates and enhancements.

You may also like

- Aeroacoustic characteristics of owl-inspired blade designs in a mixed flow fan: effects of leading- and trailing-edge serrations
Jinxin Wang, Kenta Ishibashi, Masaaki Joto et al.
- The Keck Interferometer
M. M. Colavita, P. L. Wizinowich, R. L. Akeson et al.
- Acoustic emissions from a high-speed propeller
R Soundararajan and T J S Jothi

Breath Biopsy® OMNI®
The most advanced, complete solution for global breath biomarker analysis

TRANSFORM YOUR RESEARCH WORKFLOW


Expert Study Design & Management


Robust Breath Collection

Reliable Sample Processing & Analysis


In-depth Data Analysis


Specialist Data Interpretation

This content was downloaded from IP address 145.90.34.137 on 06/02/2023 at 08:35

IOP Publishing Measurement Science and Technology
Meas. Sci. Technol. **34** (2023) 044007 (12pp) https://doi.org/10.1088/1361-6501/acb071

A wavelet-based separation method for tonal and broadband components of low Reynolds-number propeller noise

S Meloni[1,*], E de Paola[2], E Grande[3], D Ragni[3], L G Stoica[2], A Di Marco[2] and R Camussi[2]

[1] Department of Economics, Engineering, Society and Business Organization, University of Tuscia, 01100 Viterbo, VT, Italy
[2] Department of Engineering, Roma Tre University, Via Vito Volterra 72, Rome 00146, Italy
[3] Faculty of Aerospace Engineering, Delft University of Technology, Kluyverweg 1, Delft 2629 HS, The Netherlands

E-mail: stefano.meloni@uniroma3.it

Received 1 September 2022, revised 9 December 2022
Accepted for publication 5 January 2023
Published 20 January 2023

Abstract

Propeller noise generally exhibits a rich mixture of tonal and broadband components related to different physical mechanisms. Specifically, the tones are characterized by having deterministic and persistent characteristics, while the broadband counterpart has random behaviour. The separation is essential for the experimenters as they provide information on the different noise sources. In this framework, the study presents a novel wavelet-based method able to separate the noise emitted by a low Reynolds number propeller into its tonal and broadband components. The technique is applied to an isolated rotor operating under different loading configurations, including hover and cruise conditions. The acoustic pressure data are obtained in the anechoic tunnel (A-tunnel) of the TU Delft low-speed laboratory with a near-field polar and azimuthal distribution of microphones. The method is based upon a threshold varying procedure that separates the tonal and broadband components through the computation of two-point statistics. Advantages and drawbacks with respect to other methodologies already known from the literature are discussed. The application of the method provides the spectral content of the tonal and broadband components as well as the different polar and azimuthal directivity. Specifically, the observed dipole-like shape directivity for the tonal part and flatter broadband OASPL, confirm that the method can provide quite a good separation. Furthermore, the overall flow behaviour is inferred from the decomposition and validated through benchmarked flow visualizations.

Keywords: wavelet decomposition, drone, propeller noise, aeroacoustics, PIV

(Some figures may appear in colour only in the online journal)

1. Introduction

Environmental sustainability has led to the deployment of disruptive solutions for improving aircraft performance, prompting the industry and the scientific community to opt for relatively larger propeller rotors with relatively lower disk loading [1]. This has led to stronger interactions between the rotors and the supporting structures, due to the reduced distances between the propulsive unit and the airframe components. Concurrently, in the last decades, advances in electronic control systems and propulsive devices promoted the deployment of a very broad range of vehicles, from small unmanned aerial vehicles to larger urban air-mobility ones, with very

* Author to whom any correspondence should be addressed.

 © 2023 IOP Publishing Ltd

different missions [2]. The common denominator of all these vehicles is their manoeuvrability, automated stability, and the extensive range of operations including hover and vertical take-off/landing. This creates a range of turbulence interactions between rotors with the onset of tonal and broadband noise contributions that are difficult to understand and predict. Therefore, to ensure a sustainable deployment of all vehicles in urban areas, it is crucial to be able to separate and understand all physical phenomena of noise generation, in order to deploy proper strategies to mitigate the different contributions.

Studies from literature [3–6], show that many are the sources that contribute to the noise emissions from vehicles with relatively large rotors. Amongst all of them, generally the most significant is the propeller contribution, often separated into three components: harmonic or tonal noise, narrow-band noise, and broadband noise [7, 8].

The harmonic noise is determined by the blade loading and thickness contributions, which are determined by the rotational motion of the object. Therefore, propeller harmonic components are indeed expected to be integer multiples of the fundamental frequency related to the engine rotational speed. On the other hand, the broadband component is a random non-periodic contribution either determined by the trailing-edge noise scattering of the blade, or by other stochastic phenomena related to complex mechanisms, including turbulence ingestion or blade-vortex interactions, which are typically weakly correlated with the rotor revolutions per minute (RPM). The different nature of the two aforementioned components, leads to a different directivity of the acoustic emission as well as to a different noise amplitude dependency upon the scaling parameters (e.g. Reynolds number, advance ratio). Therefore, a solid understanding of each noise component is essential for modelling and predicting rotor noise, as well as for evaluating the efficacy of noise-mitigation strategies which can be later investigated by computational models. Only a few research works presented in the literature are conceived as tonal isolation techniques, and they include peak-finding algorithm, moving average curves, phase averaging, and broadband extrapolation procedures such as the Sree's Method [9–11]. An interesting example is the one of [12], in their investigation on fan noise, the authors employed a Vold–Kalman filter to extract the harmonic noise sources [13]. They concluded that a separate estimation of the tonal and broadband noise for fan noise allows for predicting propulsion-airframe integration effects. Recently Antoni *et al* [14] proposed a data-drive algorithm flexible enough to extract very large numbers of tones in a reasonable time, providing a very efficient separation when applied to counter-rotating open rotors.

The current study presents a novel wavelet-based algorithm able to separate the broadband components from acoustic signal emitted by a propeller, typically dominated by tonal noise. Due to the mathematical formulation of the wavelet transform, the method provides with the reconstruction in the physical time domain of both tonal and broadband components as separated time series. The analysis is carried out using a benchmarked database from a low Reynolds number propeller operating in hover and cruise conditions. The presented results in this manuscript focus on a subset of the full database corresponding to the benchmarked APC 9×6-based propeller ($\mathrm{Re} \approx 10^4$) tested at TU Delft in the low-speed anechoic A-tunnel. Data corresponding to two advance ratios $J = 0$ and $J = 0.4$, and different rotational velocities (4000 and 5000 RPM) are selected for the present analyses. Noise measurements were performed using a microphone array positioned in the polar and azimuthal direction on the propeller disk plane [15] while a statistical random and phase-locked analysis was carried out in the slipstream and at the blade level with planar PIV. The decomposition method has been first assessed using single and two-point statistics with the scope of verifying the procedure's validity. The extracted tonal and broadband contributions are further analyzed in terms of directivity characteristics highlighting the effects of the different propeller in-flow conditions. Finally, an empirical scaling is presented providing a satisfactory collapse of the noise amplitudes and directivity for both tonal and broadband components.

The paper is organized as follows: the experimental setup is reported in section 2, the wavelet methodology with tonal-broadband noise separation technique in section 3. Results, including the flow visualizations and the assessment of the method are discussed in section 4, whereas conclusions are reported in section 5.

2. Experimental setup

2.1. Wind tunnel and propeller rig

The experiments have been carried out in the anechoic tunnel (A-tunnel) of the low-speed laboratory of TU Delft. The A-tunnel is a vertical, open-jet wind tunnel installed in an anechoic chamber with walls covered by melamine wedges [16]. A circular exit nozzle with a diameter of 0.60 m and a contraction ratio of 15:1 has been employed for this study. The propeller used for this investigation is a benchmarked version obtained from a derivation of an APC 9×6 blade scaled up to $D = 30$ cm. For practical purposes the blade profiles have been reshaped to NACA4412 airfoil (see [15]). The propeller, made of an aluminium alloy, has been manufactured using computer numerical control machining at TU Delft with 0.4–0.8 μm Ra finish. The propeller is connected to a profiled aluminium nacelle of 5 cm diameter for minimum interference with the propeller flow. Within the nacelle, a motor, an encoder, a load cell, and a torque cell are assembled. The nacelle is supported by stiffened hollow aluminium NACA 0012 profiles of 6 cm chord, inside which all the cabling is housed and remotely connected to the instrumentation outside the jet. The entire structure is held up above the nozzle of the tunnel by four steel-wire tubes of 2 cm diameter fixed to the tunnel to minimize vibrations and interference. The propeller is driven by an electric brushless motor Leopard Hobby 3536-5T 1520 KV, with a diameter of 27.8 mm and a maximum power of 550 W. The motor is powered by a Delta Elektronika DC power supply with a voltage range of 0–15 V and a current range of 0–100 A. The motor rotational speed is measured using a US Digital EM1 optical encoder, coupled with a US Digital disk of 25.4 mm diameter and 200 cycles per revolution (1.8 deg of uncertainty on the position).

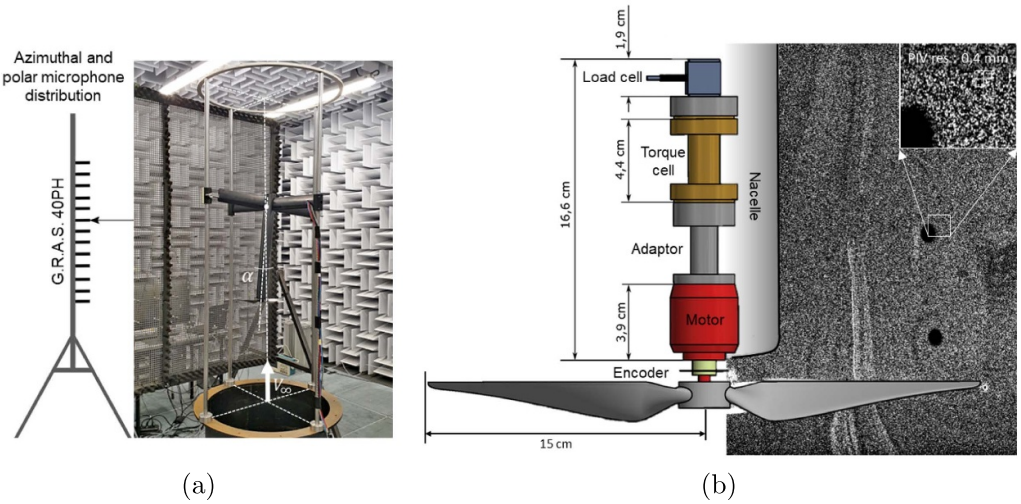

Figure 1. Details of full experimental setup in the A-tunnel: (a) microphone distribution; (b) propeller set-up.

2.2. Flow visualization and acoustic measurements

Data from the extensive stereoscopic PIV measurement campaign from Grande *et al* [15] are employed to explain the different flow interactions which contribute to the acoustic footprint, further analyzed with the wavelet decomposition method. For this study, the stereoscopic PIV measurements pertaining to the propeller slipstream, as reported in figure 1, have been used from the benchmark dataset. Detailed information about the data can be found in the study of [15]. More specifically, the flow field is seeded with particles of 1 μm median diameter produced by a SAFEX Twin Fog generator with SAFEX-Inside-Nebelfluid, a mixture of dyethelene glycol and water. Illumination of the field of view is provided by a double cavity Quantel Evergreen EVG00200 Nd:YAG laser with 200 mJ/pulse energy. To measure the flow in the propeller slipstream with sufficient resolution, data pertaining to different fields of view have been acquired. Two Imager sCMOS cameras with 2560×2160 pixels and two Nikon lenses with respectively 105 mm and 200 mm focal lengths at f# 11 have been used for the different fields of view. Sets of 500 images have been recorded and averaged to obtain the flow statistics in the slipstream and close to the propeller blade. Camera calibration, acquisition, and post-processing have been carried out with LaVision Davis 8.4 software. The images are processed with a window deformation iterative multi-grid algorithm [17] with a final interrogation window size of 24×24 pixels and 75% overlap corresponding to a maximum spatial resolution of 0.4 mm in the detailed field of view and 0.8 mm in the slipstream. Spurious vectors are isolated through a median filter and replaced by interpolation.

Acoustic measurements are carried out with a microphone distribution arranged in the horizontal and vertical directions, to obtain both polar and azimuthal directivity of the propeller noise. To the purpose 13 G.R.A.S. 40PH analogue free-field microphones are employed, having a diameter of 7 mm, a frequency range between 10 and 20 KHz, and a maximum sound pressure level (SPL) of 135 dB. The microphones are calibrated using a G.R.A.S. 42AA pistonphone with a 250 Hz pressure wave having an amplitude of 114 dB (reference sound pressure of 20 μPa). The uncertainty of the calibration is less than 0.09 dB (99 confidence level). The data acquisition system consists of a National Instrument PXIe-4499 sound and vibrations data acquisition module. The distance between each microphone is 0.5D (0.15 m), microphone 7 is at the propeller plane, microphone 1 is 3D (0.9 m) above the propeller plane, and microphone 13 is 3D below. Microphone voltages have been recorded for 30 s at a frequency rate of 50 kHz. A photograph of the experimental setup and a schematic of the propeller is additionally shown in figure 1.

3. Methodology

3.1. Wavelet analysis

The wavelet technique allows for the simultaneous representation of a temporal signal in terms of a time shift (t) and a resolution time scale (s) which inversely corresponds to the frequency (f) [18–20]. The application of the wavelet transform is performed by projecting the acquired signal onto the basis of compact support functions localized both in the time domain and in the transformed space. Formally, the wavelet transform of a time signal, in this case, the propeller pressure signal $p(t)$, is defined as the L^2 inner product between $p(t)$ and the wavelet family $\psi(t)$:

$$w(s,\tau) = s^{-1/2} \int_{-\infty}^{\infty} p(t)\psi^* \left(\frac{t-\tau}{s}\right) dt, \qquad (1)$$

where $s \in \Re^+$ is the scale dilation parameter, $\tau \in \Re$ is the translation parameter corresponding to the position of the wavelet in the physical space and $\psi^*\left(\frac{t-\tau}{s}\right)$ is the complex conjugate of the dilated and translated mother wavelet $\psi(t)$. In order to highlight the time intermittent behaviour of the detected features by removing the dependence on the local energy, the so-called local intermittency measure (LIM) [18, 21] is calculated. It represents a normalized version of the wavelet scalogram obtained by the time-frequency distribution of the

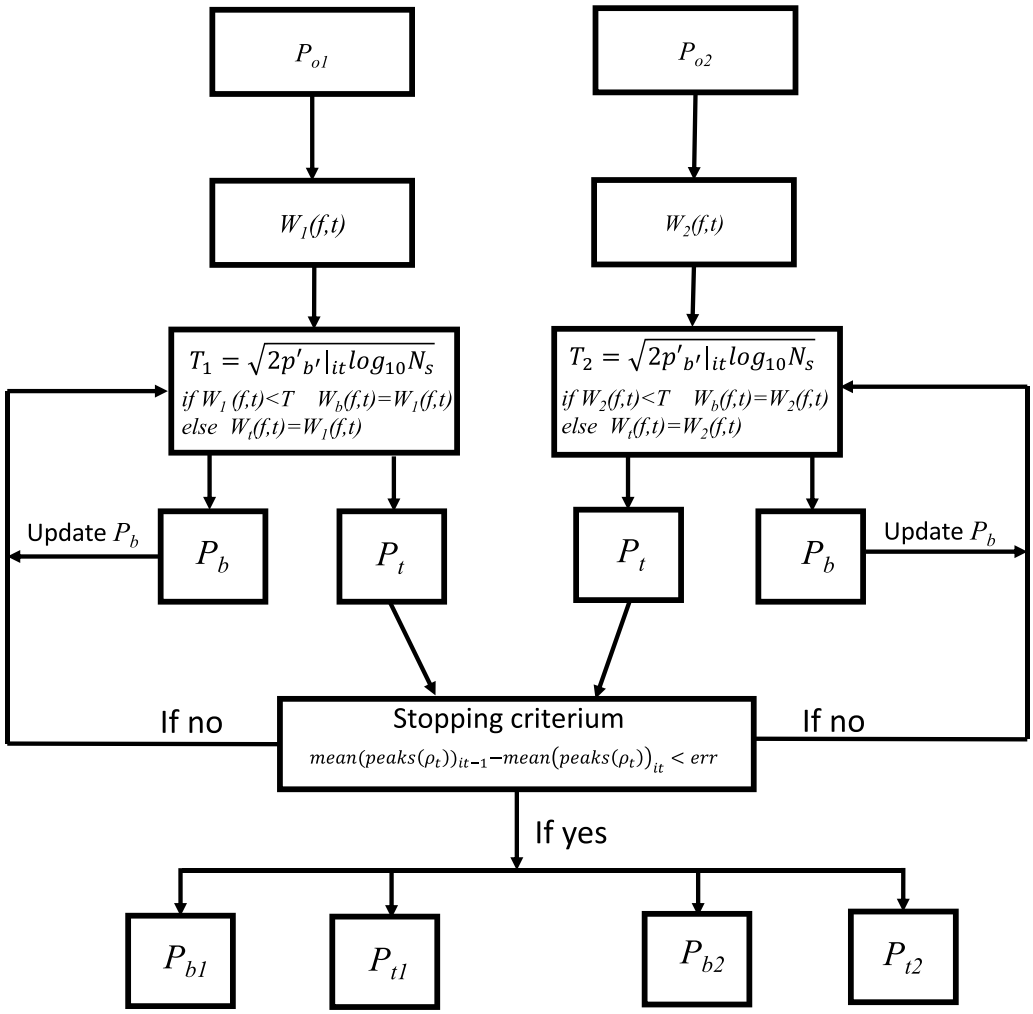

Figure 2. A schematic view of the algorithm.

square of the wavelet coefficients. The formal definition of LIM is the following:

$$\mathrm{LIM}(s,\tau) = \frac{||w(s,\tau)||^2}{\langle ||w(s,\tau)||^2 \rangle_t}, \tag{2}$$

where $|w(s,\tau)|^2$ is the local energy density and $\langle |w(s,\tau)|^2 \rangle_t$ is the average value of the energy density. The notation $\langle \ldots \rangle_t$ indicates the time average of the considered quantity. Intermittent events were identified by a LIM higher than one, while LIM lower or equal to this threshold determines the presence of signatures continuous in time.

3.2. Decomposition algorithm

The wavelet decomposition algorithm proposed in this work uses the discrete wavelet transform, which employs a discrete mother wavelet as a support function. In the presented method, two simultaneous time signals (P_o) are necessary to extract the two components because of the separation criteria based on the cross-correlation evaluation. Furthermore, acquired signals were filtered before the decomposition procedure using a high-pass frequency filter to avoid low-frequency spurious effects, localized between 0 and 40 Hz.

The procedure's first step is applying the wavelet transform, with which a matrix of the wavelet coefficients ($W(f,t)$) is obtained. This passage of the algorithm is repeated in parallel for the two signals (see figure 2). It is worth noting that for this application, the mother wavelet selection is not trivial due to the presence of harmonics features. However, according to biomedical experiences (see e.g. [22–24]) in the denoising of electrocardiogram signals, which are characterized by periodic tones, the authors employed for this application a Symlets mother wavelet [22, 25]. This nearly symmetric mother wavelet is characterized by different vanishing moments, whose value has been selected in the presented algorithm at 6 (i.e. Sym6).

The core of the procedure is the iterative process which runs according to previous works performed in different applications, e.g. [20, 22, 26], and it enables us to separate the wavelet coefficients into two sets: in this case, we assume that coefficients exceeding the threshold (T) are related to the

tonal component and those having magnitude lower than the threshold are considered representative of the broadband part. Before the first iteration, all the tonal and broadband components wavelet coefficients matrix have a pre-defined value equal to zero.

One of the non–trivial steps of this method is the definition of the threshold value. In the present study, we define the threshold level similarly to previous papers that perform wavelet denoising procedures, such as [23, 26, 27], by evaluating it as follows (see also [28]):

$$T = \sqrt{2p'_{b_{it}} \log_{10} N_s}, \tag{3}$$

where p'_b is the variance of the signal counterpart related, for this application, to the broadband component, N_s is the number of samples, and *it* identifies each iteration. In the first iteration, the variance is computed from the original signal (see figure 2). At each iteration, the presumed broadband signal is reconstructed using the inverse wavelet transform, and its variance is used to vary the threshold (see equation (3)) until a proper convergence criterion, explained below, is satisfied.

The convergence criterion is based on the computation of the cross-correlation between the presumed tonal components extracted from two consecutive microphones. Formally, the cross-correlation reads as follows:

$$R_{i,i+1} = \langle p(x,t), p(x+\xi, t+\tau) \rangle, \tag{4}$$

where ξ is the distance in the polar direction between the two consecutive microphones, τ is the time lag, and the symbol $\langle\ \rangle$ denotes a time average. The cross-correlation coefficient $\rho_{i,i+1}$ is obtained by normalizing $R_{i,i+1}$ by the product of the standard deviations of the two pressure signals.

Being the cross-correlation computed between two periodic or quasi–periodic signals, it exhibits an oscillatory trend. According to equation (5) the iterative procedure stops when the mean value of this oscillation amplitude does not vary between two consecutive iterations, as an indication of purely periodic signals.

$$\text{mean}(\text{peaks}(\rho_t))_{(it-1)} - \text{mean}(\text{peaks}((\rho_t))_{(it)} < \text{err}. \tag{5}$$

It is worth noting that to have an excellent decomposition, the error should be fixed at values about 10^{-8}. The error value is strictly connected to the number of iterations and the evaluation time, which increases by reducing the error. From the authors' experience, error values lower than 10^{-10} do not influence the number of iterations and the quality of the decomposition.

As previously mentioned, the broadband and tonal signals are eventually reconstructed in the physical space through the inverse wavelet transform. It is pointed out that the reconstruction of the tonal and broadband components as time series represents one of the main advancements with respect to existing methodologies. Based on the authors' knowledge, the most appropriate decomposition method developed in literature is the one published in [9, 11]. This procedure extracts the broadband counterpart by removing an average tonal waveform from the original signal and evaluates the tonal spectrum with subtraction in the Fourier domain. The major drawbacks of this method are that the broadband spectrum may contain irregular tone-like spikes due to unaccounted random phase shifts in the original signal, and although it is effective in the reconstructions of the tonal and broadband auto-spectra, it does not provide their counterpart in the physical domain.

4. Results

4.1. Flow statistics

In the present section, a few details regarding the mean and instantaneous flow features are reported. For a thorough description of the flow features in the slipstream and in the near vicinity of the blade the reader can refer to the study of [15]. Flow features are summarized in figure 3 where mean and instantaneous (one single snapshot) velocity and vorticity distributions are presented for the two tested advance ratios $J = 0$ and $J = 0.4$. The mean flow analysis confirms a stronger contraction of the slipstream for $J = 0$ with respect to $J = 0.4$. At the higher loading case (lower J), the vorticity distribution in the wake shows that the tip-vortex helix pitch is relatively small, approximately $0.05D$. This determines a non-negligible component of blade-vortex interaction for this specific case. To the extent of the blade wakes convected downstream by the induction field, a relatively more pronounced span-wise coherence can be appreciated for $J = 0.4$ with respect to the $J = 0$ case. The tip-vortices mutual auto-induction for $J = 0$ instead determines the breakdown of the slipstream already at less than half a rotor diameter from the propeller disk. These differences in the blade loading distributions affect the acoustic footprint, as it will be confirmed by the acoustic analysis.

4.2. Time-frequency analysis

The scalogram and LIM of segments of pressure signals obtained in hover and at low loading conditions are reported in figure 4. Plots of the phase-locked vorticity distribution, when the blade is just entering the plane, are also presented for clarity. It can be observed that three main contributions can be identified from the scalogram distribution in terms of frequency. The low frequency content is periodic and corresponds to the blade passing frequency. In the wavelet domain the trace of the periodic effect is a continuous line in the scalogram and is not evidenced in the LIM. This low frequency signature is slightly modulated by the second contribution corresponding to the rotational frequency of the electric motor [15]. As expected, the very low imbalance of the electric engine is more visible in the scalogram for the case $J = 0.4$, due to the relatively lower loading of the propeller blade. The third component is appreciated for the lower J at a relatively higher frequency, around 2 kHz. It mostly corresponds to the acoustic

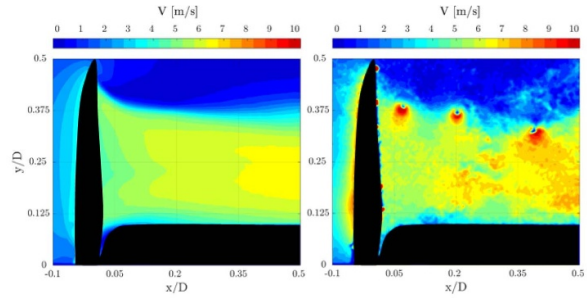

(a) *Velocity magnitude, mean(left) and instantaneous(right), J=0*

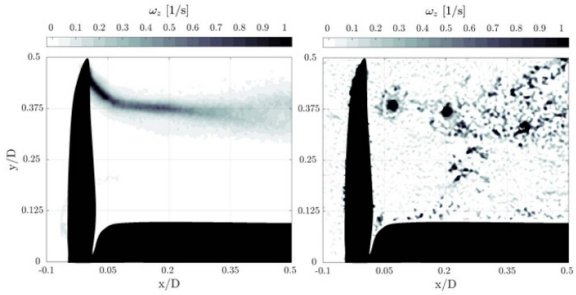

(b) *Out-of-plane vorticity, mean(left) and instantaneous(right), J=0*

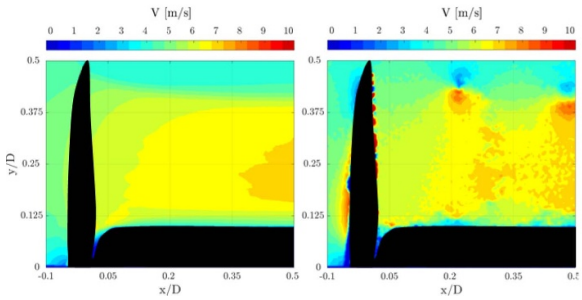

(c) *Velocity magnitude, mean(left) and instantaneous(right), J=0.4*

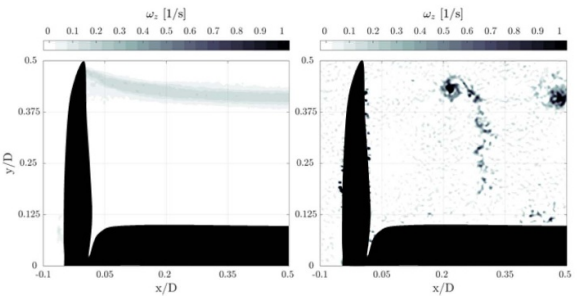

(d) *Out-of-plane vorticity, mean(left) and instantaneous(right), J=0.4*

Figure 3. Mean and instantaneous flow results for the two propeller condition $J = 0$ (first row) and $J = 0.4$.

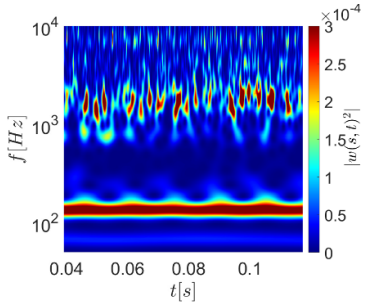

(a) *Wavelet scalograms, J=0*

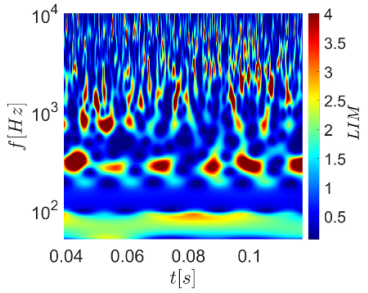

(b) *LIM contour maps, J=0*

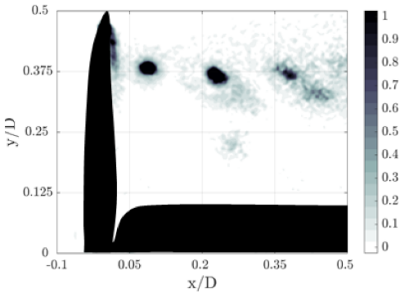

(c) *Phase-locked ω_z, J=0*

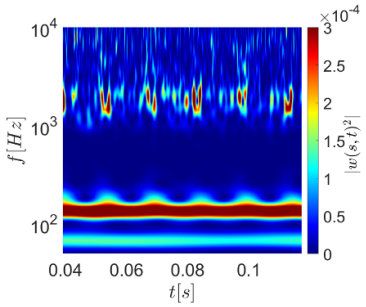

(d) *Wavelet scalograms, J=0.4*

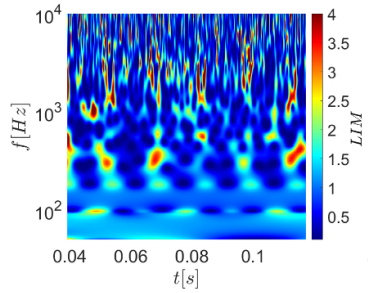

(e) *LIM contour maps, J=0.4*

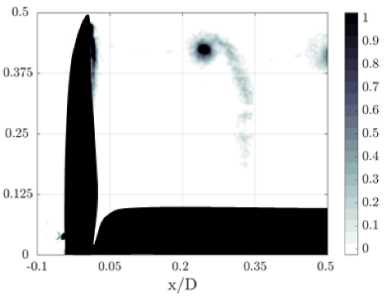

(f) *Phase-locked ω_z, J=0.4*

Figure 4. Wavelet scalograms, LIM contour maps and phase-locked out-of-plane vorticity for $J = 0$ (first row) and $J = 0.4$.

footprint of the noise produced by the coherent flow structures generated from the separated shear layer on the propeller blade (see [15]). In hover, the high frequency energy contribution is relatively more intense as an effect induced on the blade by the tip-vortex (i.e. incipient blade-vortex interaction) as shown in figure 4(c).

To the extent of the LIM distributions (figures 4(b) and (e)), the signature of the first BPF is not evident because it does not

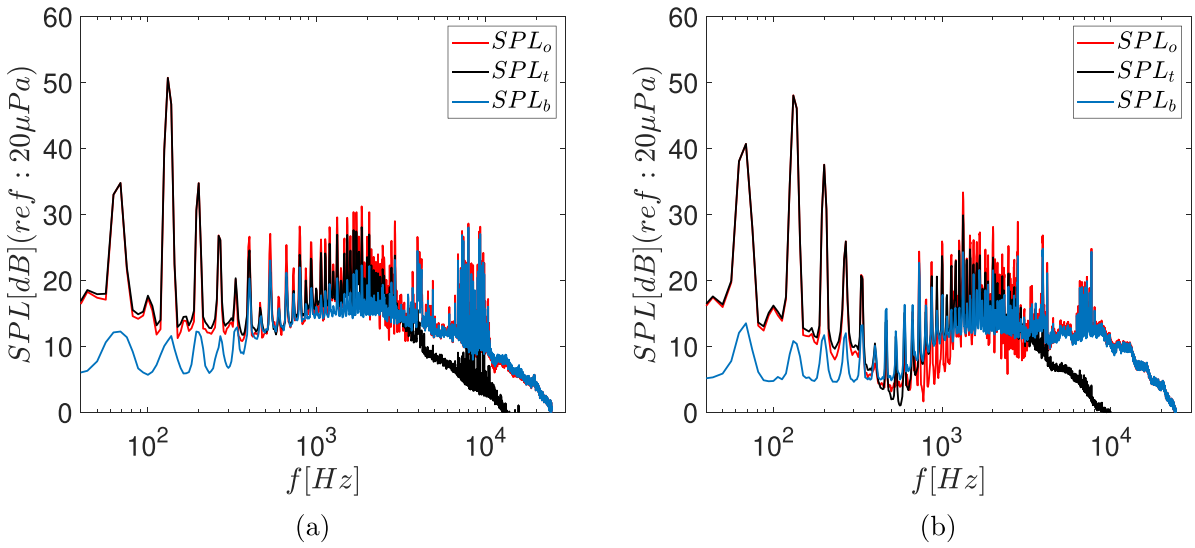

Figure 5. SPLs comparison: (a) RPM = 4000 and $U = 0\,\mathrm{m\,s^{-1}}$; (b) RPM = 4000 and $U = 8\,\mathrm{m\,s^{-1}}$. p_o denotes the spectrum of the original signal, p_t of the tonal component, p_b of the broadband component.

exhibit any intermittency. On the other hand, the LIM highlights the effect of the rotor imbalance at higher frequencies, which results quite intermittent for the propeller in hover, with a LIM amplitude between 2.5 and 3, and more persistent in time at $J = 0.4$. This indicator confirms that the reduction of the blade loading increases the time-persistency of the noise generated by the rotor imbalance. For frequencies higher than 1 kHz, the LIM behaviour is quite chaotic and intermittent, as expected for the broadband acoustic component.

4.3. Tonal and broadband decomposition of the acoustic signal

Decomposed results were analyzed by using a series of indicators. The first one is the Fourier transform in terms of SPL evaluated as follows:

$$\mathrm{SPL} = 10\log_{10}\left(\frac{\mathrm{PSD}\Delta f_{\mathrm{ref}}}{P_{\mathrm{ref}}^2}\right), \tag{6}$$

where PSD denotes the power spectral density computed using the Welch's method, Δf_{ref} is the frequency bandwidth and P_{ref} is the reference pressure in air (equal to 20 µPa).

Spectra are reported in figures 5(a) and (b) in hover and for $J = 0.4$, respectively. It is clearly noticed that the decomposition algorithm in both cases provides a satisfactory extraction of the tonal peaks related to the blade passage from the broadband region of the whole spectrum. The tonal component correctly reproduces the spectral signatures of the BPF, which are slightly perceptible in the broadband counterpart. The separation technique also extracts the tonal contribution of the motor noise that, as also reported by [15], is in the range approximately from 1 kHz to 2 kHz. As the contributions of the motor noise give a small imbalance in the loading, which is synchronized with the rotational frequency of the blades, the decomposition is appointing this effect partially in the tonal and partially in the broadband part of the signal. Additionally, from the broadband part, a clear difference can be seen between advance ratio $J = 0$ and $J = 0.4$. In the second one, the effect of the laminar separation bubble can be appreciated from the extra hump at about 2–8 kHz, also isolated by the wavelet method (see also figure 3). In the more loaded hover case, the spectra follow decay that resembles the conventional trailing edge noise at a relatively high frequency. The validity of the decomposition procedure has also been estimated in the time domain through the computation of cross-correlations(see equation (4)) between the separated tonal and broadband signals. Results are reported in figures 6(a) and (b) for the same cases of figure 5. The original signals, as expected, are characterized by pseudo periodic oscillatory trends (the red curves of figure 6). The cross-correlation of the broadband components (p_b) in both cases results stochastically uniform in time, and harmonic effects generated by the blade passing frequency are no longer observed. The tonal component is correctly extracted and provides a periodic evolution of the correlation.

The effectiveness of the separation method is even clearer for the case of non-zero advance ratio, where the harmonic oscillations in the original cross-correlation are masked by non-periodic effects but instead are well visible in the tonal counterpart (see figure 6(b)). This is explainable considering the operational regime of the propeller: in hover, the convective velocity of the tip-vortices is governed by the induction field of the propeller. Due to the relatively high loading and the low tip-vortex helix pitch, a residual contribution of the potential flow of the vortical structures on the propeller is left (very similar to BVI, see figure 3). This might determine the presence of residual harmonics in the broadband component. With the presence of a positive advance ratio, the loading is reduced as well as the strength of the tip vortices that are closer to the blade. This results in a more effective separation of the broadband and tonal contributions.

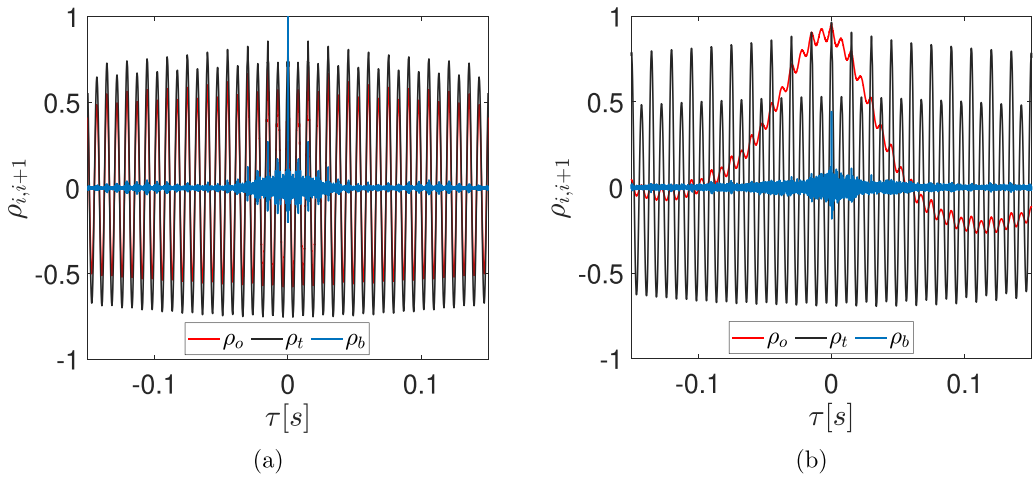

Figure 6. Cross correlation comparison: (a) RPM = 4000 and $U = 0\,\mathrm{m\,s^{-1}}$; (b) RPM = 4000 and $U = 8\,\mathrm{m\,s^{-1}}$.

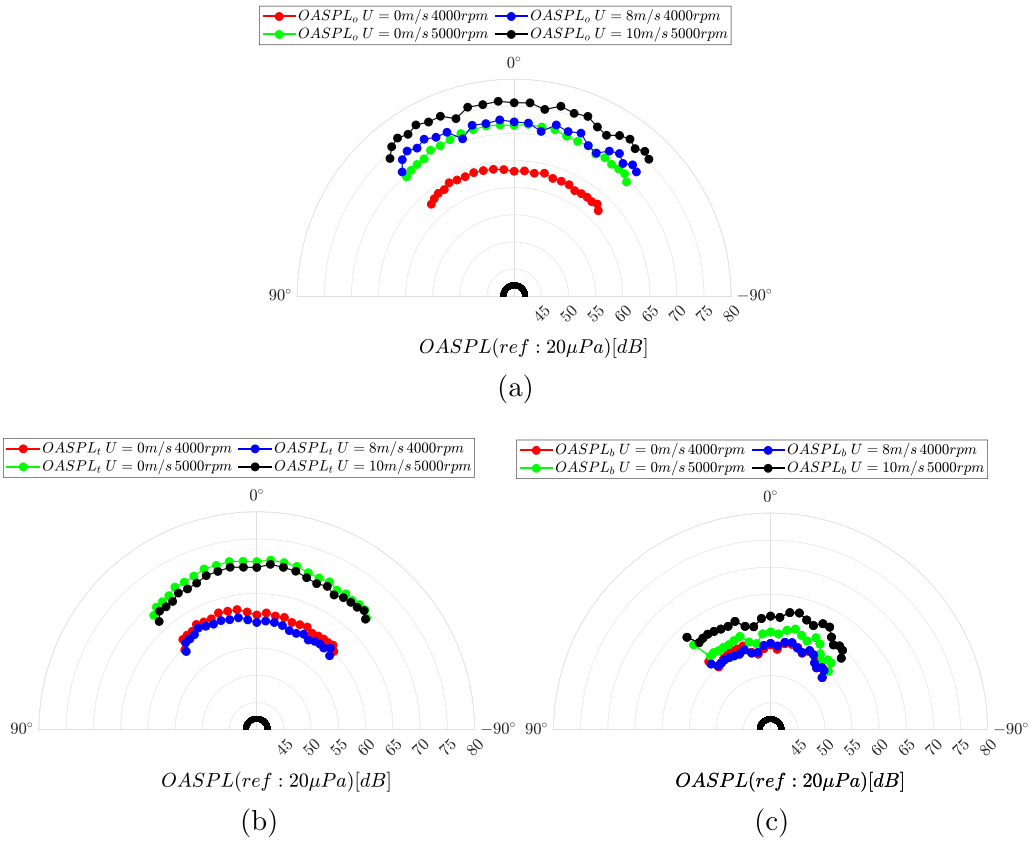

Figure 7. Azimuthal directivity: (a) original; (b) tonal; (c) broadband.

4.4. Analysis of the noise directivity

The directivity of the decomposed signals is analyzed for three cases: $J = 0$ and RPM = 4000, $J = 0.4$ and RPM = 4000, $J = 0.4$ and RPM = 5000. The directivity patterns attributed to each noise component were obtained by computing the Overall Sound Pressure Level (OASPL), defined as follows:

$$\mathrm{OASPL} = 10\log_{10}\left(\frac{p'^2}{P_{\mathrm{ref}}^2}\right), \tag{7}$$

where p'^2 is the variance of the pressure signal and p_{ref} is the reference pressure in air (equal to 20 µPa).

Figures 7 and 8 show the polar and azimuthal directivity for the original signal and the two extracted components. At $J = 0$, the original OASPL curves are dominated by the rotor noise whereas the harmonic contributions become significantly lower when the wind tunnel flow is present. At $J = 0.4$, the shape of the directivity of the original signal, in both directions, is dictated by shear layer effects induced by the wind tunnel. Figures 7(b) and 8(b) present the directivity

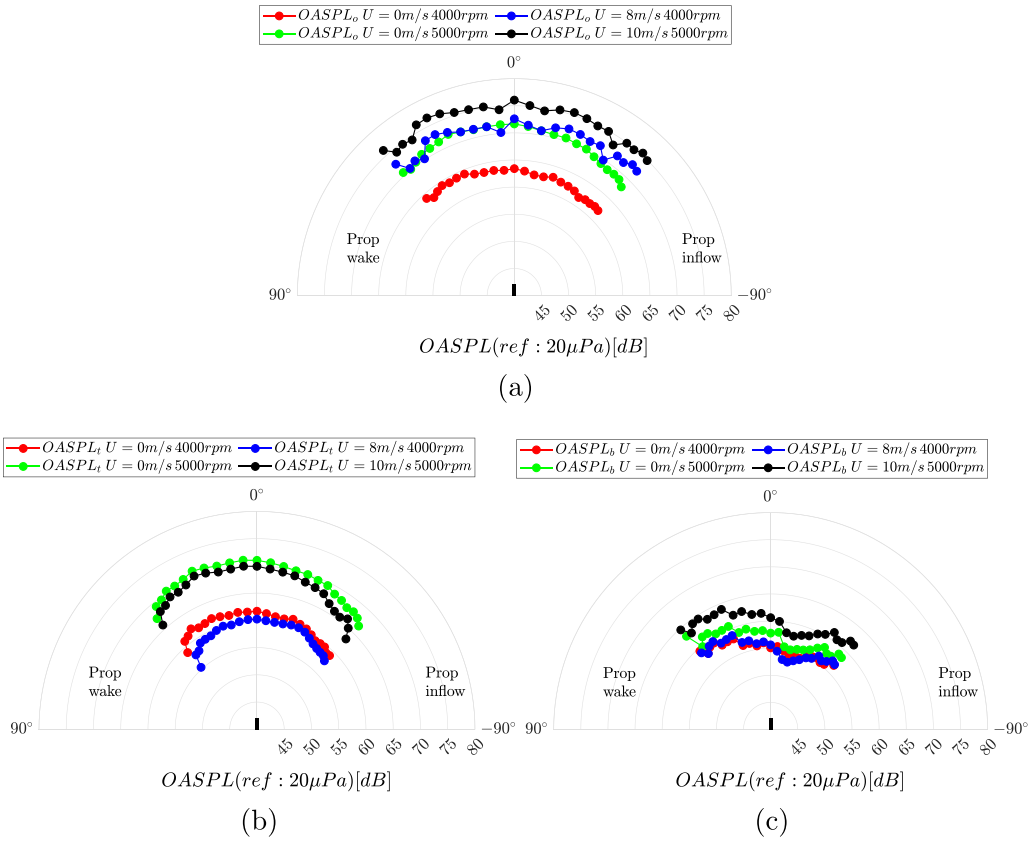

Figure 8. Polar directivity: (a) original; (b) tonal; (c) broadband.

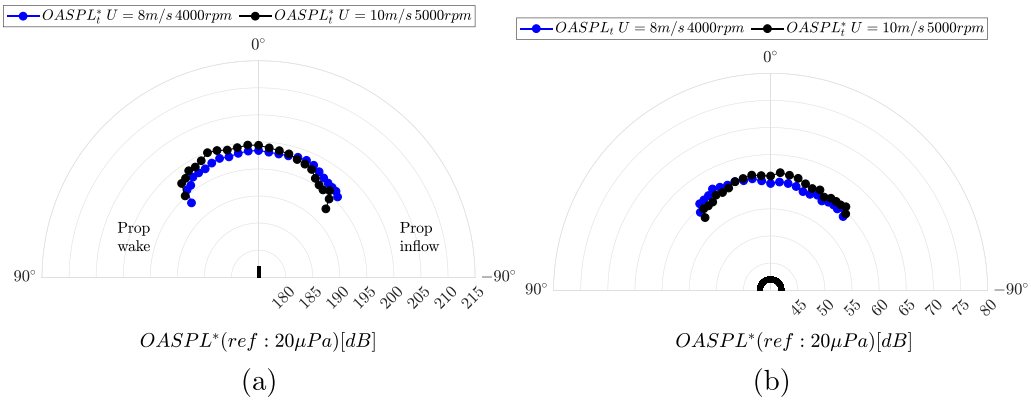

Figure 9. Empirically scaled tonal directivity: (a) polar; (b) azimuthal.

of the tonal components for both the polar and the azimuthal directions. The observed trend is very similar to the one predicted in literature (e.g. [7, 29]) where the propeller directivity is analytically represented by an array of dipoles. As expected, the tonal directivity is weakly affected by the advance ratios whereas the increase of the rotational velocity leads to a relevant amplification of the tonal noise on almost the whole polar arc. This behaviour can be ascribed to the increase of the propeller thrust. The tonal OASPL obtained from the decomposed signals in the advancing cases, can be scaled on the basis of a proper exponent of the Mach number evaluated at the tip of the blades, denoted as Mt. The scaling law that better collapses the present data is given by the following expression:

$$\mathrm{OASPL}_t^l = \mathrm{OASPL}_t^h - 20 \cdot \log_{10}\left(\frac{Mt_h}{Mt_l}\right)^{\alpha} \tag{8}$$

where OASPL_t is evaluated from the tonal counterpart of the decomposed signal, Mt_h and Mt_l are the tip Mach numbers for the higher and lower rotating velocity propeller, respectively, and the exponent α is taken equal to 4.5. As shown in figure 9 the directivity well scale with M_t by using 4.5 as

exponent. Indeed, a good collapse of the curves is observed, with a maximum error lower than 2 dB in both azimuthal and polar directions. According to the literature [7], the exponent 4.5 suggests that the physics of the tonal counterpart can be related to the blade thickness and loading contributions.

Considering the broadband components directivity, a distribution quite different with respect to the tonal one is observed. The polar directivity (figure 8(c)) indicates that the energy is larger in the wake region downstream of the propeller probably as an effect of the blades vortex noise. This asymmetry is less evident in the azimuthal directivity (figure 7(c)), since the wake effects do not influence it. It should be stressed that the conclusions obtained from the directivity analyses could not be driven by the original signals (see figures 7(a) and 8(a)) because of the presence of the broadband component that affects significantly the directivity patterns and intensity.

5. Conclusion

A wavelet-based analysis able to separate the tonal and the broadband components of the noise emitted by a low-Reynolds propeller has been presented. The database employed consisted of a series of measurements from the benchmarked propeller carried out in [15], including near-field acoustic pressures with the rotor in hover and cruise conditions. The interpretation of the wavelet results has been related to the already available flow statistics of the propeller, measured with stereoscopic PIV. The wavelet-time frequency analysis has been used to connect the acoustic footprint with the differences in blade loading distributions observed in the flow-field. The main advantage of this new method is the reconstruction in the physical domain of the tonal and broadband pressure components. Furthermore, the presented procedure is completely automatic with a reasonable computational time. The assessment of the decomposition in terms of Fourier spectra shows tones in the tonal counterpart with only slight traces in the broadband component. The analysis in the physical domain performed using the cross-correlation function highlighted the oscillatory pseudo periodic trends in the tonal part that are much more evident with respect to the cross-correlation of the original signals. The effectiveness of the wavelet-based separation procedure is more evident in in-flight configuration, where the BPF oscillations are masked by the wind tunnel shear layer effects. The directivity of the separated tonal and broadband components are determined by the computation of the OASPL and are compared to results obtained from the original signal. A dipole-like shape has been observed for the tonal part, whereas the broadband counterpart exhibits a flatter OASPL that increases in the propeller wake zone because of the presence of blade vortex noise. The tonal component OASPL has been observed to decrease in the advancing configuration proportionally to the reduction of the loading noise due to the thrust reduction. On the other hand, the broadband component strongly increases at a positive advance ratio as an effect of the laminar separation bubble. An empirical scaling law based on the blade trailing edge noise has been used for the tonal counterpart in the advancing case, providing a good collapse.

By the end, the assessment proved that the presented separation procedure provides efficient results when an isolated propeller has been considered. However, the appraisal of the extraction procedure on different propeller noise scenarios, such as installed propeller, will be the topic of sequel research.

Data availability statement

The data generated and/or analysed during the current study are not publicly available for legal/ethical reasons but are available from the corresponding author on reasonable request.

Acknowledgments

The work is supported by the European Union's Horizon 2020 research and innovation program under Project ENODISE (Enabling optimized disruptive airframe-propulsion integration concepts) Grant Agreement No. 860103.

Appendix

To better understand the advantages of the presented method, a comparison with the phase averaging procedure, which is well-assessed and widely used in the literature, has been shown in this appendix. It is worth noting that the phase averaging method is able to reconstruct the tonal component time series without providing any information in the physical domain for the broadband counterpart. Therefore, to be consistent, only the extracted tonal component have been compared in figure 10.

Similar results in terms of tonal spectra were observed between the two methods at the low and mid frequencies. On the other hand, at frequencies higher than 3 kHz, there is a substantial difference. Specifically, some broadband contribution still remains in the tonal counterpart when using phase averaging. This is more evident in the advancing case due to the higher level of broadband generated by the separation bubbles. In addition, peaks related to the motor noise (see frequencies between 8–10 kHz) are accounted for in the tonal component extracted by the phase averaging procedure, this is partially incorrect, being this noise source not related to the propeller cyclostationary noise. A further comparison has been reported in the physical domain by cross-correlating two consecutive tonal components extracted using the two methods (see figure 11). The higher harmonic oscillations in wavelet separated case testify to a more in-depth removal of the broadband component. This difference is accentuated in the advancing case. In conclusion, the presented method can improve the results obtained by phase averaging by providing a better separated tonal component, without any reduction of

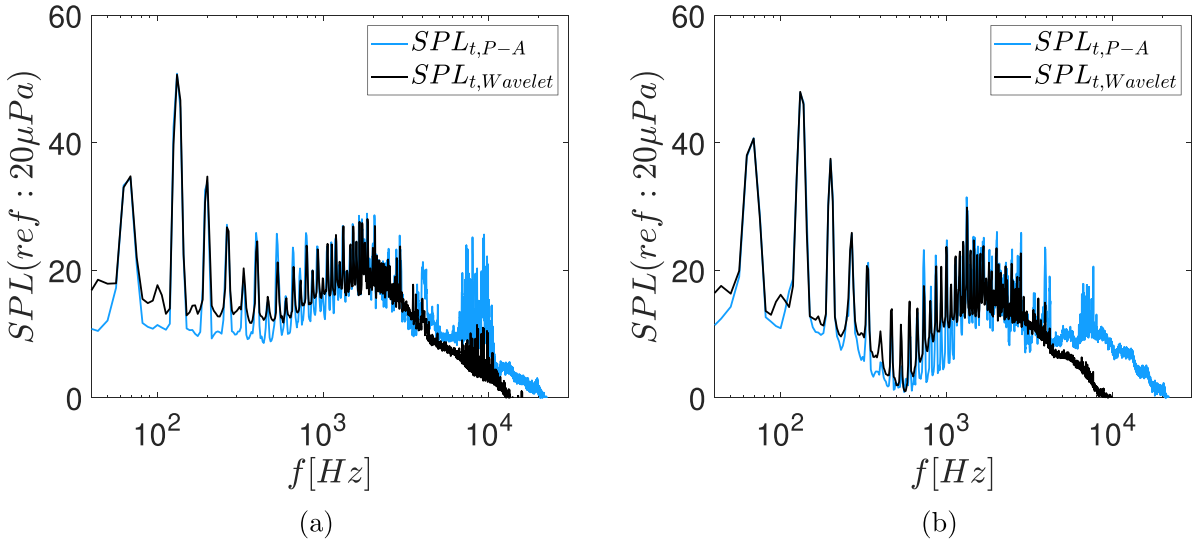

Figure 10. Tonal SPLs comparison: (a) RPM = 4000 and $U = 0\,\mathrm{m\,s^{-1}}$; (b) RPM = 4000 and $U = 8\,\mathrm{m\,s^{-1}}$. p_o denotes the spectrum of the original signal, $p_{t,P-A}$ of the tonal component evaluated using the phase-averaging method, $p_{t,\mathrm{wavelet}}$ of the tonal component evaluated using the wavelet approach.

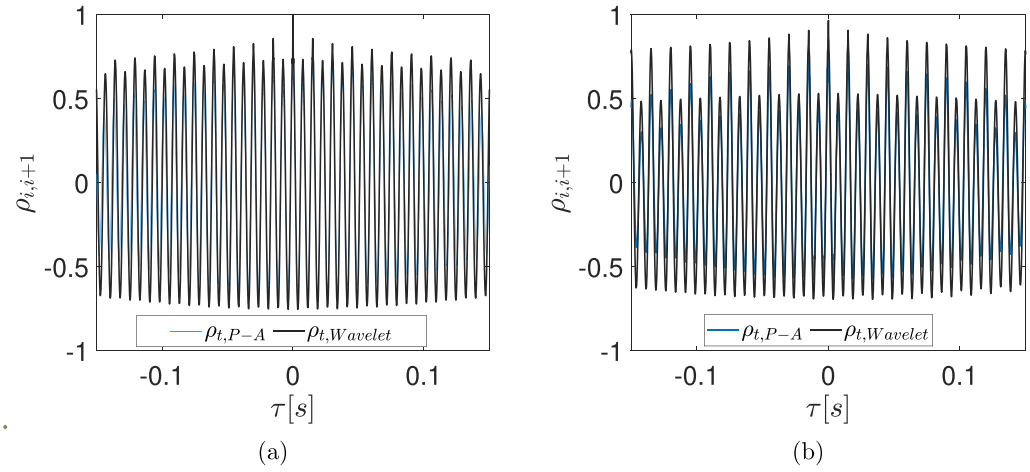

Figure 11. Cross correlation comparison: (a) RPM = 4000 and $U = 0\,\mathrm{m\,s^{-1}}$; (b) RPM = 4000 and $U = 8\,\mathrm{m\,s^{-1}}$.

the number of samples and by carrying out the time series of the broadband component.

ORCID iDs

S Meloni https://orcid.org/0000-0003-1532-7463
D Ragni https://orcid.org/0000-0002-8014-5650

References

[1] Casalino D, Diozzi F, Sannino R and Paonessa A 2008 Aircraft noise reduction technologies: a bibliographic review *Aerosp. Sci. Technol.* **12** 1–17
[2] Coykendal J, Metcalfe M, Hussain A and Dronamraju T 2022 Advanced air mobility: disrupting the future of mobility *Deloitte Papers*
[3] Dahan C, Avezard L, Guillien G, Malarmey C and Chombard J 1980 Propeller light aircraft noise at discrete frequencies *J. Aircr.* **18** 480–6
[4] Massey K and Gaeta R 2010 Noise measurements of tactical UAVs *16th AIAA/CEAS Aeroacoustics Conf.* p AIAA 2010-3911
[5] Sinibaldi G and Marino L 2013 Experimental analysis on the noise of propellers for small uav *Appl. Acoust.* **74** 79–88
[6] Intaratep N, Alexander W N, Devenport W J, Grace S M and Dropkin A 2016 Experimental study of quadcopter acoustics and performance at static thrust conditions *22nd AIAA/CEAS Aeroacoustics Conf.* p AIAA 2016-2973
[7] Hubbard H H 1991 *Aeroacoustics of Flight Vehicles: Theory and Practice* NASA Reference Publication 1258, NASA Report
[8] Smith M J T 1989 *Aircraft Noise* (*Cambridge Aerospace Series*) (Cambridge: Cambridge University Press)
[9] Sree D 2013 A novel signal processing technique for separating tonal and broadband noise components from counter-rotating open-rotor acoustic data *Int. J. Aeroacoust.* **12** 169–88
[10] Stephens D and Sree D 2014 Tone and broadband noise separation from acoustic data of a scale-model counter-rotating open rotor *20th AIAA/CEAS Aeroacoustics Conf.* (https://doi.org/10.2514/6.2014-2744)

[11] Sree D and Stephens D B 2016 Improved separation of tone and broadband noise components from open rotor acoustic data *Aerospace* **3** 29
[12] Truong A and Papamoschou D 2015 Harmonic and broadband separation of noise from a small ducted fan *21st AIAA/CEAS Aeroacoustics Conf.* (https://doi.org/10.2514/6.2015-3282)
[13] Kingan M, Blandeau V, Tester B, Joseph P and Parry A 2011 Relative importance of open rotor tone and broadband noise sources *17th AIAA/CEAS Aeroacoustics Conf.* (*32nd AIAA Aeroacoustics Conf.*) (https://doi.org/10.2514/6.2011-2763)
[14] Antoni J, Leclère Q, Dinsenmeyer A, Julliard E, Bouley S, Picard C and Sijtsma P 2022 Standalone extraction of tonal components from aeroacoustic signals *AIAA J.* **60** 844–59
[15] Grande E, Romani G, Ragni D, Avallone F and Casalino D 2022 Aeroacoustic investigation of a propeller operating at low Reynolds numbers *AIAA J.* **60** 860–71
[16] Merino-Martínez R, Rubio Carpio A, Lima Pereira L T, van Herk S, Avallone F, Ragni D and Kotsonis M 2020 Aeroacoustic design and characterization of the 3D-printed, open-jet, anechoic wind tunnel of Delft University of Technology *Appl. Acoust.* **170** 107504
[17] Ooi A, Martin J, Soria J and Chong M S 1999 A study of the evolution and characteristics of the invariants of the velocity-gradient tensor in isotropic turbulence *J. Fluid Mech.* **381** 141–74
[18] Farge M 1992 Wavelet transforms and their applications to turbulence *Annu. Rev. Fluid Mech.* **24** 395–458
[19] Meloni S, Lawrence J L, Proença A R, Self R H and Camussi R 2020 Wall pressure fluctuations induced by a single stream jet over a semi-finite plate *Int. J. Aeroacoust.* **19** 240–53
[20] Camussi R and Meloni S 2021 On the application of wavelet transform in jet aeroacoustics *Fluids* **6** 299
[21] Meloni S and Kamliya Jawahar H 2022 A wavelet-based time-frequency analysis on the supersonic jet noise features with chevrons *Fluids* **7** 108
[22] Li W 2019 Wavelets for electrocardiogram: overview and taxonomy *IEEE Access* **7** 25627–49
[23] Lin H Y, Liang S Y, Ho Y L, Lin Y H and Ma H P 2014 Discrete-wavelet-transform-based noise removal and feature extraction for ECG signals *IRBM* **35** 351–61
[24] Smith C, Agaian S and Akopian D 2008 A wavelet-denoising approach using polynomial threshold operators *IEEE Signal Process. Lett.* **15** 906–9
[25] Meloni S, de Paola E, Grande E, Ragni D, Georgiana Stoica L, di Marco A and Camussi R 2022 Wavelet-based decomposition of the tonal-broadband components of propeller noise *28th AIAA/CEAS Aeroacoustics 2022 Conf.* (https://doi.org/10.2514/6.2022-2876)
[26] Ruppert-Felsot J, Farge M and Petitjeans P 2009 Wavelet tools to study intermittency: application to vortex bursting *J. Fluid Mech.* **636** 427–53
[27] Donoho D L and Johnstone I M 1994 Ideal spatial adaptation by wavelet shrinkage *Biometrika* **81** 425–55
[28] Mancinelli M, Pagliaroli T, Di Marco A, Camussi R and Castelain T 2017 Wavelet decomposition of hydrodynamic and acoustic pressures in the near field of the jet *J. Fluid Mech.* **813** 716–49
[29] Brentner K S and Farassat F 2003 Modeling aerodynamically generated sound of helicopter rotors *Prog. Aerosp. Sci.* **39** 83–120